

SPACECRAFT ANGULAR RATE ESTIMATION ALGORITHMS FOR STAR TRACKER-BASED ATTITUDE DETERMINATION

Puneet Singla,^{*} John L. Crassidis,[†] John L. Junkins[‡]

In this paper, two different algorithms are presented for the estimation of spacecraft body angular rates in the absence of gyro rate data for a star tracker mission. In first approach, body angular rates are estimated with the spacecraft attitude using a dynamical model of the spacecraft. The second approach makes use of a rapid update rate of star camera to estimate the spacecraft body angular rates independent of spacecraft attitude. Essentially the image flow of the stars is used to establish a Kalman filter for estimating the angular velocity. The relative merits of both the algorithms are then studied for the spacecraft body angular rates measurements. The second approach has an advantage of being free from any bias in attitude estimates.

Introduction

Spacecraft angular rate data plays an important role in attitude determination and attitude control. With the use of rate data, the attitude of spacecraft can be predicted between two different frames of star tracker data. Generally, three axis gyros are used on board to provide the body angular rate information. In the presence of densely measured rate data, the exact kinematic model can replace the dynamical model. But when rate data is not available, then estimation accuracy is obviously dependent on 1) accuracy of the star measurements, 2) their frequency in time, and 3) the accuracy of the dynamical model. An accidental gyro failure (e.g. failure of four of six rate gyros on the Earth Radiation Budget Satellite¹) or intentionally omission of gyros (e.g. in Small Explorer (SAMPEX)¹) due to their high cost can necessitate “gyroless” attitude estimation. The loss of gyro data can result in unacceptably high propagation errors.

The problems related to spacecraft attitude estimation in loss of gyro data has been discussed by Mook,¹ and he proposed an estimation algorithm, which can in principle take

^{*}Graduate Student, Aerospace Engineering, Texas A&M University, College Station, TX 77843-3141,puneet@tamu.edu.

[†]Assistant Professor, Department of Aerospace and Mechanical Engineering, University at Buffalo, State University of New York, Amherst, NY 14260-4400, Tel: (716) 645-2593, johnc@eng.buffalo.edu.

[‡]George J. Eppright Chair Professor, Director of the Center for Mechanics and Control, Fellow AAS, Department of Aerospace Engineering, Texas A&M University, College Station, TX 77843-3141,Tel: (979) 845-3912, Fax: (979) 845-6051,junkins@tamu.edu.

care of both inaccurate rate data and inaccurate dynamic model. He suggested that the Minimum Model Error (MME) approach to be used to obtain the most accurate state estimate for poorly modelled dynamic systems by taking into account the error in model dynamics. Afterwards these MME estimates may be used for model identification. Crassidis and Markley² have obtained accurate estimates for the SAMPEX spacecraft by using only magnetometer sensor measurements. But the disadvantages with the MME based approach is that it falls into the category of batch estimation (i.e., all the data should be processed simultaneously), which significantly restricts its use in real time applications. The Kalman filter is an ideal choice for real time applications. However, the accuracy of the Kalman filter estimation depends in a complicated way upon the accuracy of dynamic model and tuning of the process noise covariance matrix. So between two sets of measurements, the estimates are still subjected to accumulation of model error. It should be noted that the Kalman filter does consider model error, but virtually all implementations consider the model error to be a “white noise random process”. This model usually inadequate to represent colored (correlated) model errors; for the case of poorly known systematic (non-white) model errors, the MME and related algorithms are more attractive. While MME methods enjoy some theoretical advantages, both the Kalman filter and MME algorithms require tuning, however the required artistic tuning of the Kalman filter algorithms are in a more mature state of development. Fisher et. al.³ discussed the use of the Kalman filter for attitude and angular rate determination using attitude sensor outputs alone.

Sufficient information about the body angular rates can be obtained from the attitude sensor measurements, if attitude sensor data frequency is fast enough to capture the spacecraft motion. Star cameras are very accurate and, in view of recent active pixel sensor cameras, star camera frame rates are increasingly high. This suggests the possibility of deriving angular velocity measurements from “star motion” on the focal plane. In this paper, two different sequential algorithms will be presented for spacecraft body angular rates estimation in the absence of gyro rate data for a star tracker mission.

1. In the first approach, body angular rates of spacecraft will be estimated with spacecraft attitude using the Kalman filter. This method uses a dynamical model in which, external torques acting on spacecraft are modelled by random walk process. So the performance of this algorithm will depend on the validity of assumed dynamical model for the given case.
2. The second approach makes use of the rapid update rate of the star camera to approximate body angular velocity vector independent of attitude estimation. A time derivative of star tracker body measurements is taken to establish “measurement equations” for estimating angular velocity. First order and second order finite difference approaches will be used to approximate the time derivative of body measurements. A sequential Least Squares algorithm is used to estimate the spacecraft angular rates. This algorithm works fine, if the sampling interval of star data is well within Nyquist’s limit for the actual motion of the spacecraft.

The structure of this paper proceeds as follows. First a brief review of star tracker model is given. The subsequent section introduces the attitude dependent angular velocity

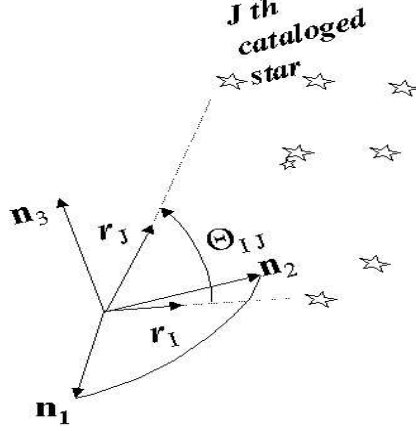


Figure 1 Catalog Star Pair

estimation followed by the attitude independent approach. Finally, computer simulation results are presented to test the algorithms.

Star Tracker Model

Star positions are a very accurate source as the reference system for the attitude determination problem as their position is fixed with respect to inertial system fixed to earth. Spacecraft attitude is determined by taking the photographs of the star by a star camera. Pixel formats of the order of 512×512 or larger are commonly used to provide good resolution pictures. The first stage in attitude determination is to identify the stars with reference to on-board catalog. Star catalog contain the spherical co-ordinate angles of the stars (α is the right ascension and δ is the declination, Figure 1) to a high accuracy.

Many algorithms have been developed for the star identification.⁴ All star identification algorithms can be divided into three categories: 1) Direct match, 2) Angular separation match, and 3) Phase match. Star identification algorithm based upon the Angular separation approach are very popular.⁵ After star identification is made, image plane coordinates of the stars are given by using a pinhole camera model for the star camera. Photograph image plane coordinates of j^{th} star are given by following co-linearity equations:

$$x_j = f \frac{C_{11}r_{x_j} + C_{12}r_{y_j} + C_{13}r_{z_j}}{C_{13}r_{x_j} + C_{32}r_{y_j} + C_{33}r_{z_j}} + x_0 \quad (1)$$

$$y_j = f \frac{C_{21}r_{x_j} + C_{22}r_{y_j} + C_{23}r_{z_j}}{C_{13}r_{x_j} + C_{32}r_{y_j} + C_{33}r_{z_j}} + y_0 \quad (2)$$

where f is the effective focal length of the star camera and (x_0, y_0) are principal point offsets, determined by the ground or on-orbit calibration, C_{ij} are the direction cosines

matrix elements, and the inertial vector \mathbf{r}_j is given by

$$\mathbf{r}_j = \begin{Bmatrix} r_{x_j} \\ r_{y_j} \\ r_{z_j} \end{Bmatrix} = \begin{Bmatrix} \cos \delta_j \cos \alpha_j \\ \cos \delta_j \sin \alpha_j \\ \sin \delta_j \end{Bmatrix} \quad (3)$$

choosing the z-axis of the image coordinate system towards the boresight of the star camera as shown in Figure 2, the measurement unit vector \mathbf{b}_j is given by following equation:

$$\mathbf{b}_j = \frac{1}{\sqrt{x_j^2 + y_j^2 + f^2}} \begin{Bmatrix} -(x_j - x_0) \\ -(y_j - y_0) \\ f \end{Bmatrix} \quad (4)$$

The relationship between measured star direction vector \mathbf{b}_j in image space and their

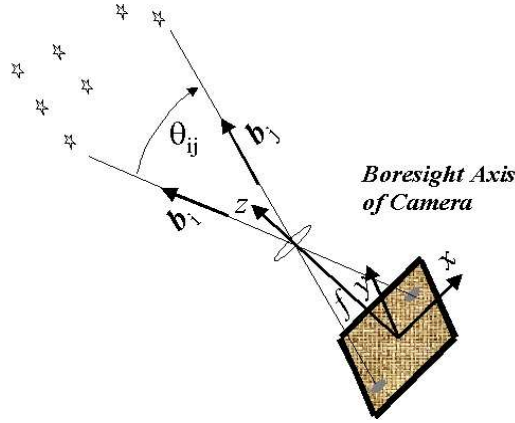


Figure 2 Image Plane Star Pair

projection \mathbf{r}_j on the inertial frame is given by

$$\mathbf{b}_j = \mathbf{C}\mathbf{r}_j + \boldsymbol{\nu}_j \quad (5)$$

where \mathbf{C} is the attitude direction cosine matrix denotes the mapping between image and inertial frame and $\boldsymbol{\nu}_j$ is a zero mean Gaussian white noise process with covariance \mathbf{R}_j .

Attitude Dependent Angular Velocity Estimation Algorithm

In this approach, the spacecraft body angular rate are estimated with spacecraft attitude using the Kalman filter. Actually, this algorithm has been derived from the attitude determination algorithm presented in ref.⁶ The state vector of the Kalman filter consists of 3 component of angular velocity in place of the rate bias vector as in.⁶

$$\mathbf{x} = \begin{Bmatrix} \delta \mathbf{q} \\ \boldsymbol{\omega} \end{Bmatrix} \quad (6)$$

The angular acceleration of the spacecraft is modelled by first order random process.

$$\boldsymbol{\tau} = \dot{\boldsymbol{\omega}} = \boldsymbol{\eta}_2 \quad (7)$$

where $\boldsymbol{\eta}_2$ represents a Gaussian random variable with the following known statistical properties:

$$\mathbf{E}(\boldsymbol{\eta}_2) = 0 \quad (8)$$

$$(\boldsymbol{\eta}_2 \boldsymbol{\eta}_2^T) = \sigma_v^2 \mathbf{I} \quad (9)$$

Therefore, the state equations for new state vector are given as:

$$\dot{\mathbf{x}} = \mathbf{F}\mathbf{x} + \mathbf{G}\mathbf{w} \quad (10)$$

where \mathbf{w} is a noise vector defined as:

$$\mathbf{w} = \begin{Bmatrix} \boldsymbol{\eta}_1 \\ \boldsymbol{\eta}_2 \end{Bmatrix} \quad (11)$$

and matrix \mathbf{F} and \mathbf{G} are given by following equations.⁷

$$\mathbf{F} = \begin{bmatrix} -\tilde{\boldsymbol{\omega}}(t) & -\frac{1}{2}\mathbf{I}_{3 \times 3} \\ \mathbf{O}_{3 \times 3} & \mathbf{O}_{3 \times 3} \end{bmatrix} \quad (12)$$

$$\mathbf{G} = \begin{bmatrix} \frac{1}{2}\mathbf{I}_{3 \times 3} & \mathbf{O}_{3 \times 3} \\ \mathbf{O}_{3 \times 3} & \mathbf{I}_{3 \times 3} \end{bmatrix} \quad (13)$$

Adopting the procedure described in refs.,^{6,7} the state propagation and update equations for Kalman filter can be written as:

Propagation Equations

$$\hat{\mathbf{q}}_{k+1} = [\cos(\frac{\theta_k}{2})\mathbf{I}_{4 \times 4} + \sin(\frac{\theta_k}{2})\boldsymbol{\Omega}(\hat{\mathbf{n}}_k)]\hat{\mathbf{q}}_k \quad (14)$$

where

$$\theta_k = \omega_n * (t_{k+1} - t_k) \text{ and } \omega_n = \|\hat{\boldsymbol{\omega}}_k\| = \sqrt{\hat{\omega}_{k1}^2 + \hat{\omega}_{k2}^2 + \hat{\omega}_{k3}^2}$$

$$\mathbf{P}_{k+1} = \boldsymbol{\Phi}_k \mathbf{P}_k \boldsymbol{\Phi}_k^T + \mathbf{G} \mathbf{Q}_k \mathbf{G}^T \quad (15)$$

with

$$\boldsymbol{\Phi}_k = \begin{bmatrix} \boldsymbol{\Phi}_{1k} & \boldsymbol{\Phi}_{2k} \\ \mathbf{O}_{3 \times 3} & \mathbf{I}_{3 \times 3} \end{bmatrix} \quad (16)$$

$$\boldsymbol{\Phi}_{1k} = \mathbf{I}_{3 \times 3} + \frac{\tilde{\boldsymbol{\omega}}^T}{\omega_n} \sin \theta_k + \left(\frac{\tilde{\boldsymbol{\omega}}^T}{\omega_n}\right)^2 (1 - \cos \theta_k) \quad (17)$$

$$\boldsymbol{\Phi}_{2k} = \frac{1}{2}[\mathbf{I}_{3 \times 3} \Delta t + \frac{(\tilde{\boldsymbol{\omega}}^T (1 - \cos \theta_k))}{\omega_n^2} + \frac{\tilde{\boldsymbol{\omega}} \tilde{\boldsymbol{\omega}}^T (\theta_k - \sin \theta_k)}{\omega_n^3}] \quad (18)$$

Update Equations

$$\hat{\mathbf{x}}_k^+ = \hat{\mathbf{x}}_k^- + \mathbf{K}_k (\tilde{\mathbf{y}}_k - \mathbf{H}_k \hat{\mathbf{x}}_k^-) \quad (19)$$

$$\mathbf{P}_k^+ = (\mathbf{I} - \mathbf{K}_k \mathbf{H}) \mathbf{P}_k^- \quad (20)$$

$$\mathbf{K}_k = \mathbf{P}_k^- \mathbf{H}_k^T (\mathbf{H}_k \mathbf{P}_k^- \mathbf{H}_k^T + \mathbf{R}_k)^{-1} \quad (21)$$

where

$$\mathbf{H}_k = [\mathbf{L} \quad \mathbf{O}_{3 \times 3}] \quad (22)$$

$$\mathbf{L} = 2[\hat{\mathbf{b}} \otimes] \quad (23)$$

Simulations

Using the J-2000 star catalog with stars of visual magnitude brighter than $M_v \sim 6.4$, assuming $8^0 \times 8^0$ FOV star camera and 17μ radian (for 1024×1024 pixel array) of centroiding error, star data are simulated at a frame rate frequency of 10Hz. Three different test cases were considered. For the first case the spacecraft is assumed to be in LEO orbit with true angular velocity, $\omega = \{ 0 \ 0.0011 \ 0 \}^T$.

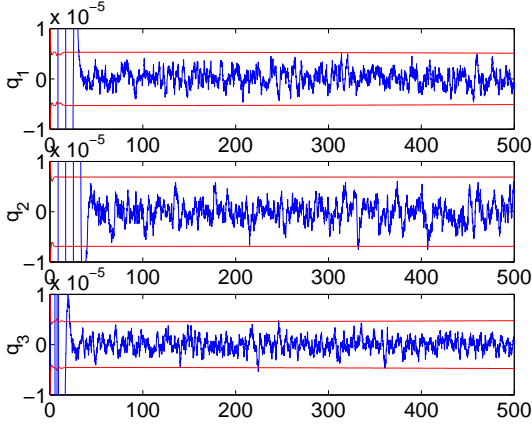


Figure 3 Attitude Errors (rad) vs Time (sec)

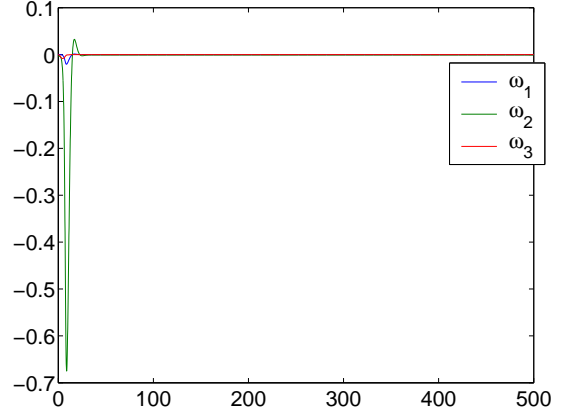


Figure 4 Estimated Spacecraft Angular Velocity (rad/sec) vs Time (sec)

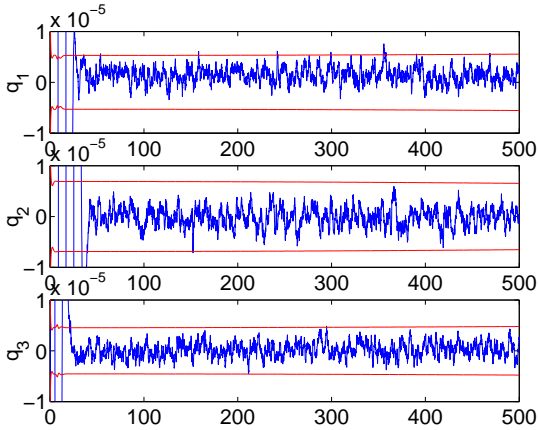


Figure 5 Attitude Errors (rad) vs Time (sec)

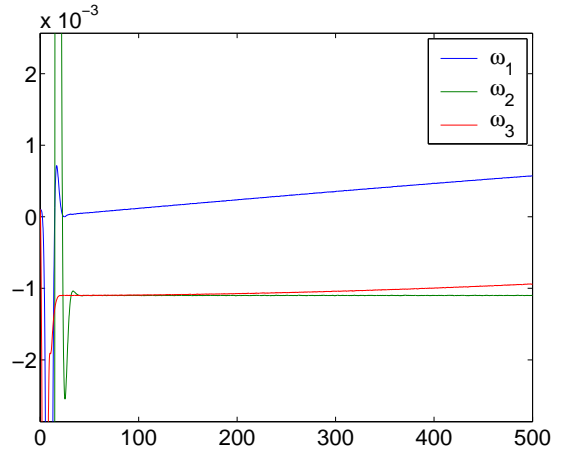


Figure 6 Estimated Spacecraft Angular Velocity (rad/sec) vs Time (sec)

Figures 3 and 4 show the plots of estimated spacecraft attitude and spacecraft angular velocities, respectively. From Figure 4 it is clear that the algorithm is able to estimate the angular velocity and attitude precisely, but the attitude estimates are somewhat less accurate as compared to the estimates when angular rates are available.

For the second test case, it is assumed that spacecraft angular velocity has small slowly time varying oscillations about the x and z axes but has a constant velocity of 0.0011 rad/sec about the y -axis. Figures 5 and 6 show the plots of estimated angular velocities and attitudes of the spacecraft respectively. From the plots, we can infer that algorithm given in this section is able to estimate the attitude and angular velocities of the spacecraft successfully even in the absence of rate data. However, the estimates are sensitive to “dropout” when sparse star regions are encountered, where star-id confidence may be too low.

For the third test case, it is assumed that spacecraft angular velocity has fast time varying angular oscillations about the x and z axes but has a constant velocity of 0.0011 rad/second about the y -axis. But unfortunately, for third test case this algorithm fails, i.e., the estimated errors are significantly outside their 3σ bounds as the angular velocities are rapidly changing with time.

The main disadvantage associated with this approach is that angular rate estimates are subject to any error in spacecraft attitude estimates and vice-versa.

Attitude Independent Approach

In this section, a deterministic approach will be used to determine the spacecraft body angular rate vector from the star tracker body measurements. This approach makes use of the increasingly rapid update rates of modern star cameras and finite different analysis of “image flow” trajectories of the measured star line of sight vectors in the sensor coordinate system. Consider the following focal plane trajectory of line of sight vector for i^{th} star $\mathbf{b}_i(t)$:

$$\mathbf{b}_i(t) = \frac{1}{\sqrt{x_i(t)^2 + y_i(t)^2 + f^2}} \begin{Bmatrix} -(x_i(t) - x_0) \\ -(y_i(t) - y_0) \\ f \end{Bmatrix} \quad (24)$$

where $x_i(t)$ and $y_i(t)$ dictate the focal plane trajectory of i^{th} star. Now, the true flow velocity measurement model is given by

$$\frac{d\mathbf{b}_i(t)}{dt} = \frac{d\mathbf{C}(t)}{dt} \mathbf{r}_i \quad (25)$$

Using the fact that $\frac{d\mathbf{C}(t)}{dt} = -[\boldsymbol{\omega}(t) \otimes] \mathbf{C}(t)$, we can rewrite equation (25) as:

$$\frac{d\mathbf{b}_i(t)}{dt} = -[\boldsymbol{\omega}(t) \otimes] \mathbf{b}_i(t) \quad (26)$$

The first order Taylor series expansion for line of sight vector for i^{th} star at time t_k is given by:

$$\mathbf{b}_i(k) = \mathbf{b}_i(k-1) + \left. \frac{d\mathbf{b}_i(t)}{dt} \right|_{k-1} \Delta t + O(\Delta t^2) \quad (27)$$

Using the fact that $\tilde{\mathbf{b}}_i(k) = \mathbf{b}_i(k) + \boldsymbol{\nu}$ and substituting for $\frac{d\mathbf{b}_i(t)}{dt}$ from equation (26), we obtain the following finite difference approximation:

$$\mathbf{Y}_i(k) = \frac{1}{\Delta t} [\tilde{\mathbf{b}}_i(k) - \tilde{\mathbf{b}}_i(k-1)] = [\tilde{\mathbf{b}}_i(k-1) \otimes] \boldsymbol{\omega}(k-1) + \mathbf{w}_i(k) + O(\Delta t) \quad (28)$$

where the effective measurement error $\mathbf{w}_i(k)$ of $\mathbf{Y}_i(k)$ is:

$$\mathbf{w}_i(k) = \frac{1}{\Delta t}[\boldsymbol{\nu}_i(k) - \boldsymbol{\nu}_i(k-1)] + [\boldsymbol{\omega}(k-1) \otimes] \boldsymbol{\nu}_i(k-1) \quad (29)$$

From equation (29), it is clear that new noise vector $\mathbf{w}_i(k)$ is a function of angular rate vector $\boldsymbol{\omega}(k-1)$. Assuming a stationary noise process for $\boldsymbol{\nu}_i$, the following covariance relationship can be easily derived

$$\mathbf{E}(\mathbf{w}_i(k)\mathbf{w}_i^T(k)) = [\boldsymbol{\omega}(k-1) \otimes] \mathbf{R}_i [\boldsymbol{\omega}(k-1) \otimes]^T + \frac{1}{\Delta t} [\mathbf{R}_i [\boldsymbol{\omega}(k-1) \otimes] - [\boldsymbol{\omega}(k-1) \otimes] \mathbf{R}_i] + \frac{2}{\Delta t^2} \mathbf{R}_i \quad (30)$$

If the sampling interval is well within Nyquist's limit i.e. $\|\boldsymbol{\omega}\|\Delta t \leq \pi$, with a safety factor of 10 then $\|\boldsymbol{\omega}\|\Delta t \leq \frac{\pi}{10}$. Since, $\|[\boldsymbol{\omega}(k-1) \otimes]\| \approx \|\boldsymbol{\omega}\|$, then the following inequalities are true

$$\|[\boldsymbol{\omega}(k-1) \otimes] \mathbf{R}_i [\boldsymbol{\omega}(k-1) \otimes]^T\| < \frac{\pi^2}{100\Delta t^2} \|\mathbf{R}_i\| \ll \frac{2}{\Delta t^2} \|\mathbf{R}_i\| \quad (31)$$

$$\|\frac{1}{\Delta t} [\mathbf{R}_i [\boldsymbol{\omega}(k-1) \otimes] - [\boldsymbol{\omega}(k-1) \otimes] \mathbf{R}_i]\| < \frac{2\pi}{10\Delta t} \|\mathbf{R}_i\| < \frac{2}{\Delta t^2} \|\mathbf{R}_i\| \quad (32)$$

It should be noted that second term of noise covariance matrix vanishes for the isotropic measurement errors (i.e. when \mathbf{R}_i is scalar times identity matrix). Therefore the last term in equation (30) dominates the first two terms, which can effectively be ignored. Equation (28) can now be cast into a Kalman filter formulation, which leads to

$$\hat{\boldsymbol{\omega}}(k)^+ = \hat{\boldsymbol{\omega}}(k)^- + \mathbf{K}_k(\mathbf{Y}_i(k) - \mathbf{H}_k \hat{\boldsymbol{\omega}}(k)^-) \quad (33)$$

where

$$\mathbf{Y}_i(k) = \frac{1}{\Delta t} [\tilde{\mathbf{b}}_i(k) - \tilde{\mathbf{b}}_i(k-1)] \quad (34)$$

$$\mathbf{H}_k = [\tilde{\mathbf{b}}_i(k-1) \otimes] \quad (35)$$

To take care of time varying angular rates we need to propagate the error covariance matrix according to the Ricatti equation. Therefore, again modelling the spacecraft angular rates by a first order statistical process, we get following propagation equations

$$\dot{\boldsymbol{\omega}} = \boldsymbol{\eta} \ \& \ \mathbf{E}(\boldsymbol{\eta}\boldsymbol{\eta}^T) = \sigma^2 \mathbf{I} \quad (36)$$

$$\mathbf{P}_k^- = \mathbf{P}_{k-1}^+ + \mathbf{G}\mathbf{Q}\mathbf{G} \quad (37)$$

where

$$\mathbf{G} = \mathbf{I}_{3 \times 3} \quad (38)$$

$$\mathbf{Q} = \sigma^2 \mathbf{I}_{3 \times 3} \Delta t \quad (39)$$

Therefore, only knowledge of the body vector measurements and sampling time interval is required to derive an angular velocity estimate.

We can improve the accuracy of spacecraft angular velocity estimates particularly for higher angular rates by considering a higher order finite-difference where the Taylor series truncation errors are of magnitude $O(\Delta t^2)$ as compared to $O(\Delta t)$ in equation (28)

$$\mathbf{Y}_i(k) = \frac{1}{2\Delta t} [4\tilde{\mathbf{b}}_i(k-1) - 3\tilde{\mathbf{b}}_i(k-2) - \tilde{\mathbf{b}}_i(k)] = [\tilde{\mathbf{b}}_i(k-2) \otimes] \boldsymbol{\omega}(k-2) + \mathbf{w}_i(k) + O(\Delta t^2) \quad (40)$$

where

$$\mathbf{w}_i(k) = [\tilde{\mathbf{b}}_i(k-2) \otimes] \boldsymbol{\nu}_i(k-2) + \frac{1}{2\Delta t} [4\boldsymbol{\nu}_i(k-1) - 3\boldsymbol{\nu}_i(k-2) - \boldsymbol{\nu}_i(k)] \quad (41)$$

Again assuming a stationary noise process for $\boldsymbol{\nu}_i(k)$, the following covariance relationship can be derived

$$\mathbf{E}(\mathbf{w}_i(k) \mathbf{w}_i^T(k)) = [\boldsymbol{\omega}(k-2) \otimes] \mathbf{R}_i [\boldsymbol{\omega}(k-2) \otimes]^T + \frac{3}{2\Delta t} [\mathbf{R}_i [\boldsymbol{\omega}(k-2) \otimes] - [\boldsymbol{\omega}(k-2) \otimes] \mathbf{R}_i] + \frac{13}{2\Delta t^2} \mathbf{R}_i \quad (42)$$

If the sampling interval is well within Nyquist's limit i.e. $\|\boldsymbol{\omega}\| \Delta t \leq \pi$, with a safety factor of 10 then $\|\boldsymbol{\omega}\| \Delta t \leq \frac{\pi}{10}$. Since, $\|[\boldsymbol{\omega}(k) \otimes]\| \approx \|\boldsymbol{\omega}\|$, then the following inequalities are true

$$\|[\boldsymbol{\omega}(k-2) \otimes] \mathbf{R}_i [\boldsymbol{\omega}(k-2) \otimes]^T\| < \frac{\pi^2}{100\Delta t^2} \|\mathbf{R}_i\| \ll \frac{13}{2\Delta t^2} \|\mathbf{R}_i\| \quad (43)$$

$$\|\frac{3}{2\Delta t} [\mathbf{R}_i [\boldsymbol{\omega}(k-2) \otimes] - [\boldsymbol{\omega}(k-2) \otimes] \mathbf{R}_i]\| < \frac{6\pi}{20\Delta t} \|\mathbf{R}_i\| < \frac{13}{2\Delta t^2} \|\mathbf{R}_i\| \quad (44)$$

again the second term vanishes for isotropic measurement errors and therefore the last term in equation (42) dominates the first two terms, which can be ignored. Equation (40) can also be cast into a Kalman filter formulation, which leads to

$$\hat{\boldsymbol{\omega}}(k)^+ = \hat{\boldsymbol{\omega}}(k)^- + \mathbf{K}_k (\mathbf{Y}_i(k) - \mathbf{H}_k \hat{\boldsymbol{\omega}}(k)^-) \quad (45)$$

where

$$\mathbf{Y}_i(k) = \frac{1}{2\Delta t} [4\tilde{\mathbf{b}}_i(k+1) - 3\tilde{\mathbf{b}}_i(k) - \tilde{\mathbf{b}}_i(k+2)] \quad (46)$$

$$\mathbf{H}_k = [\tilde{\mathbf{b}}_i(k) \otimes] \quad (47)$$

The covariance matrix \mathbf{P} can be propagated according to equation (37).

It should be noted that the second order approach has a order of magnitude less Taylor series truncation error than the first order approach but at the price of an increased standard deviation in the effective measurement noise (by a factor of $\sqrt{13}/2$). But, the Kalman filter is inadequate to represent the truncation error whereas it can treat the effective measurement noise as "Gaussian white noise process". Therefore, we expect second order approach to give better results than the first order approach whenever truncation error dominate the increase in effective measurement error which is the case for high angular velocities.

Simulations

Using the J-2000 star catalog with stars of magnitude up to 6.0, assuming $8^0 \times 8^0$ field of view star camera and 17μ radian (for 1024×1024 pixel array) of centroiding error, star data are simulated at a frame rate frequency of 10Hz. Three different test cases defined above were considered.

Figures 7 and 9 show the plots of the true angular velocity and the estimated spacecraft angular velocities from the first order and second order approaches, respectively for the first test case. Figures 8 and 10 show the plots of the corresponding spacecraft angular velocity error with 3σ bounds for the first order and second order approaches, respectively.

From these plots, it is clear that the second order approach is able to estimate the angular velocity more accurately than the first order approach.

Similarly, Figures 11 and 13 show the plots of the true and estimated spacecraft angular velocity for the second test case, by first and second order approach respectively. Figures 12 and 14 show the corresponding angular velocity error and 3σ bounds plots for first and second order approach respectively. From these plots, it is again clear that the second order approach is able to estimate the angular velocity more accurately than the first order approach. This can be due to the fact that the extra information provided by the second order approach for the star trajectory compensate for an increased standard deviation in the estimate noise.

Figures 15 and 16 show the plots of the true and estimated spacecraft angular velocity and spacecraft angular velocity error with 3σ bound by first order approach for the third test case. From the plots, it is clear that for this test case the angular velocity errors are significantly outside their 3σ bound when the magnitude of fairly changing angular velocities is high. Where as, from figures 17 and 18, we can notice that second order attitude independent algorithm works fine even for fairly high magnitude rapidly changing angular velocities case. This can be due to the fact that the second order approach not only gives better approximation of the star trajectory for rapidly changing angular velocity case but also compensate for an increased standard deviation in the estimate noise.

From the plots, we can infer that algorithm based upon the second order approach gives more accurate results for higher angular rates but surprisingly by, at the price of an increased standard deviation in the estimate noise (by a factor of $\sqrt{13}/2$).

Concluding Remarks

The important issue in this paper is to address angular rate estimation for attitude determination in case of gyro failure which increases the domain of practical applicability of attitude estimation algorithms. As usual, the convergence of the Kalman Filter depends jointly upon: 1) the accuracy of the dynamical model and process noise representation, 2) the frequency and accuracy of the attitude measurements. For the attitude independent approach, approximations of the derivatives of the “image flow” trajectories of individual stars (imaged in high frame rate cameras) gives more accurate rate estimation results than the usual Kalman filter with typical modelling errors. The main advantage of the attitude independent algorithm is that now our spacecraft body rate estimates are free from any error in attitude estimates. The second order attitude independent algorithm gives better results than the first order approach for high magnitude angular rate case. However, the second-order approach requires two time steps ahead to estimate the angular velocity at the current time (i.e., knowledge of \mathbf{b}_i at the $k + 2$ step is required to estimate $\boldsymbol{\omega}$ at the k step). The first-order approach requires only one-time step ahead. For this reason the first-order approach should be used when possible.

REFERENCES

1. D. J. Mook, "Robust Attitude Determination without Rate Gyros," *Proceedings of the AAS/GSFC International Symposium on Space Flight Dynamics*, No. 93-299, NASA-Goddard Space Center, Greenbelt, MD, April 1993.
2. J. L. Crassidis and F. L. Markely, "A Minimum Model Error Approach For Attitude Estimation," *Journal of Guidance, Control and Dynamics*, Vol. 20, No. 6, Nov. -Dec. 1997, pp. 1241-1247.
3. H. L. Fisher, M. D. Shuster, and T. E. Strikwedra, "Attitude Determination For The Star Tracker Mission," *AAS/AIAA Astrodynamics Conference*, AAS, Stowe, VT, 7 Aug-10 Aug 1989.
4. J. M. Sidi, *Spacecraft Dynamics and Control*, Cambridge University Press, Cambridge, UK.
5. D. Mortari, J. L. Junkins, and M. Samaan, "Lost-In-Space Pyramid Algorithm for Robust Star Pattern Recognition," *Guidance and Control Conference*, No. 01-004, AAS, Breckenridge, Colorado, 31 Jan- 4Feb 2001.
6. P. Singla, T. D. Griffith, and J. L. Junkins, "Attitude Determination and On-Orbit Autonomous Calibration of Star Tracker For GIFTS Mission," *AAS/AIAA Space Flight Mechanics Meeting*, No. 02-101, AAS, San-Antonio, TX, 27 Jan- 30 Jan 2002.
7. P. Singla, "A New Attitude Determination Approach using Split Field of View Star Camera," *Masters Thesis report*, Aerospace Engineering, Texas A&M University, College Station, TX, USA.

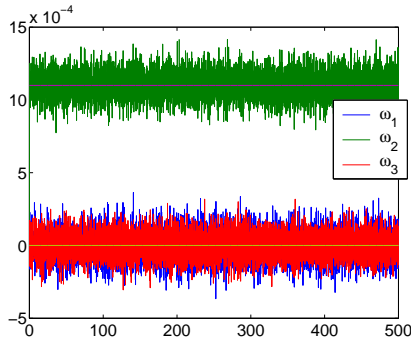


Figure 7 True and Estimated Spacecraft Angular Velocity (rad/sec) Obtained by 1st Order Approach for Test Case 1

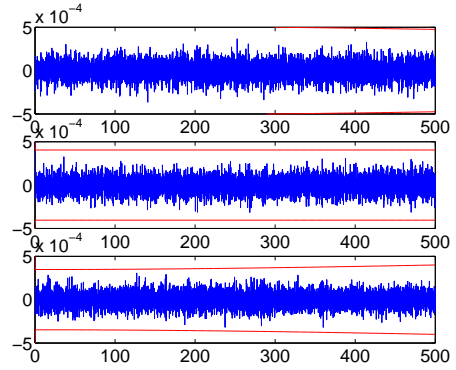


Figure 8 Estimated Spacecraft Angular Velocity Errors and 3σ Bound Obtained by 1st Order Approach for Test Case 1

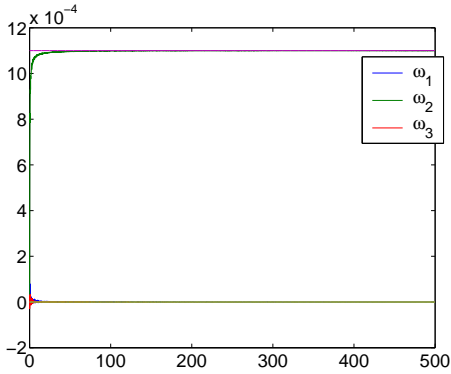


Figure 9 True and Estimated Spacecraft Angular Velocity (rad/sec) Obtained by 2nd Order Approach for Test Case 1

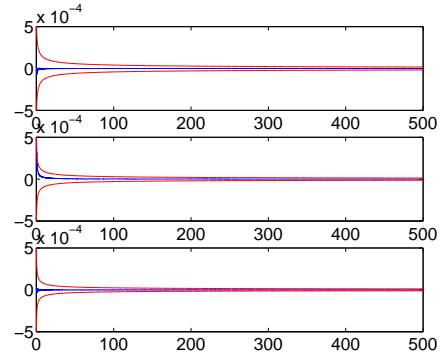


Figure 10 Estimated Spacecraft Angular Velocity Errors and 3σ Bound Obtained by 2nd Order Approach for Test Case 1

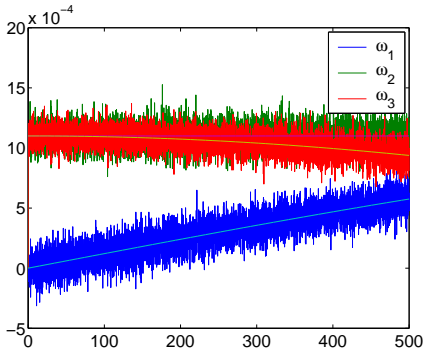


Figure 11 True and Estimated Spacecraft Angular Velocity (rad/sec) Obtained by 1st Order Approach for Test Case 2

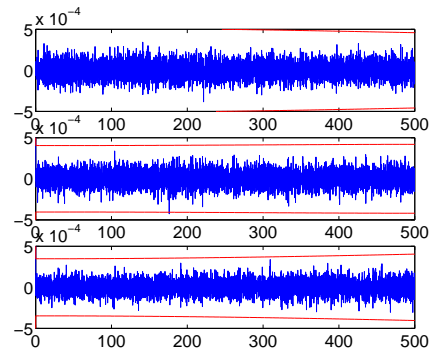


Figure 12 Estimated Spacecraft Angular Velocity Errors and 3σ Bound Obtained by 1st Order Approach for Test Case 2

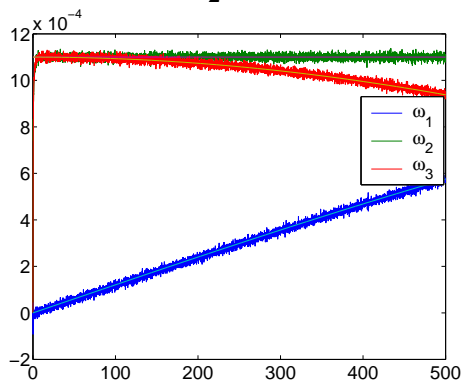


Figure 13 True and Estimated Spacecraft Angular Velocity (rad/sec) Obtained by 2nd Order Approach for Test Case 2

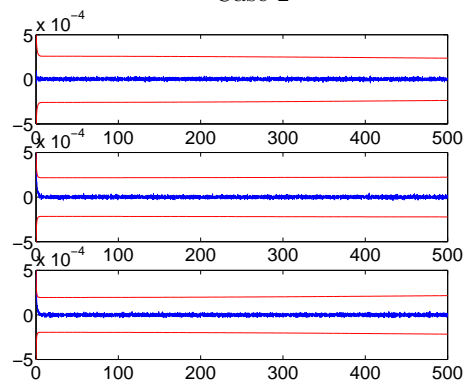


Figure 14 Estimated Spacecraft Angular Velocity Errors and 3σ Bound Obtained by 2nd Order Approach for Test Case 2

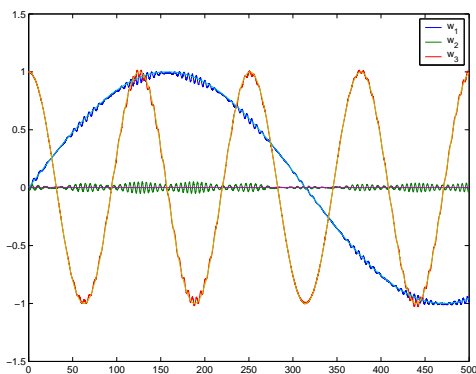


Figure 15 True and Estimated Spacecraft Angular Velocity (rad/sec) Obtained by 1st Order Approach for Test Case 3

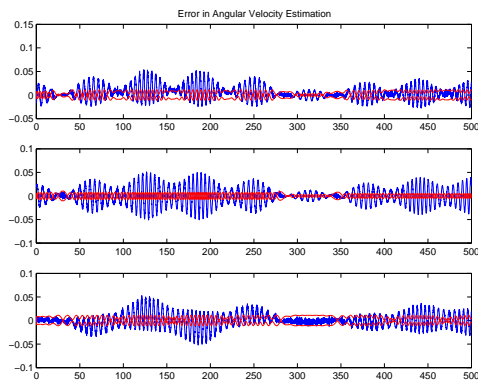


Figure 16 Estimated Spacecraft Angular Velocity Errors and 3σ Bound Obtained by 2nd Order Approach for Test Case 3

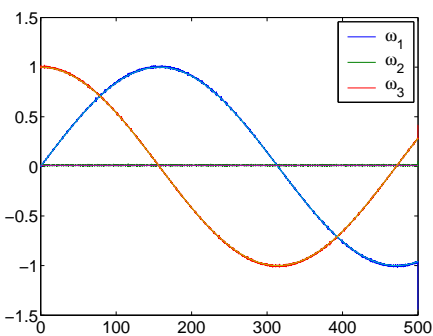


Figure 17 True and Estimated Spacecraft Angular Velocity (rad/sec) Obtained by 2nd Order Approach for Test Case 3

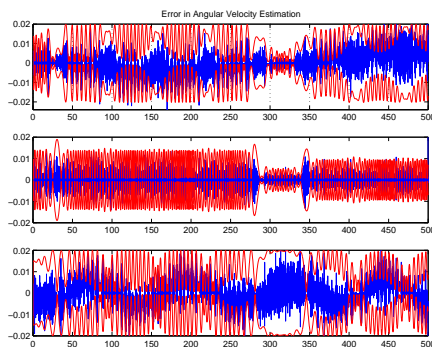


Figure 18 Estimated Spacecraft Angular Velocity Errors and 3σ Bound Obtained by 2nd Order Approach for Test Case 3